JOURNAL OF AIRCRAFT
Vol. 37, No. 5, September–October 2000

Helical-Groove and Circular-Trip Effects on Side Force

K. B. Lua,* T. T. Lim,[†] and S. C. Luo[‡]
National University of Singapore, Singapore 119260, Republic of Singapore
and
E. K. R. Goh[§]
DSO National Laboratories, Singapore 118230, Republic of Singapore

When a slender body, such as a missile, is pitched at high angle of attack to an oncoming flow, it may experience a large side force due to the asymmetric shedding of the tip vortices. The side force is well known to be highly detrimental to the performance of the flight vehicle. We assess the effectiveness of two control devices, namely, the circular trips and the helical grooves, in alleviating the side force on a tangent ogive nose cylinder. Simultaneous side force and pressure measurements taken in a wind tunnel show that the circular trip is generally more effective in reducing the side force than the helical grooves over a wide range of angle of attack. Detailed findings of their performances are reported.

Nomenclature

Cp = pressure coefficient, $(P - P_\infty)/(0.5\rho U_\infty^2)$
Cy = side force coefficient, $Fy/(0.5\rho U_\infty^2 S)$
$Cy(X)$ = local side force coefficient, local side force/$(0.5\rho U_\infty^2 D \sin^2 \alpha)$
D = cylinder diameter
Fy = side force
L = length of body
P = pressure on model surface
P_∞ = freestream static pressure
Re_D = Reynolds number, $U_\infty D/\nu$
S = model base area, $\pi D^2/4$
U_∞ = freestream velocity
X = axial distance from nose tip
α = angle of attack
δ_N = tip semi-apex angle
θ = azimuth angle around circular cross section measured from the most leeward position
ν = kinematics viscosity of fluid
ρ = density of fluid
ϕ = roll angle

I. Introduction

MODERN aircraft and missile are required to operate agilely at high angles of attack. However, operating under this condition can lead to several adverse effects. A notable one is the generation of a large side force on the forebody, even when the flight vehicle is at zero side slip. The side force, which can be as large as 1.5 times the normal force,[1,2] has been attributed by many to the asymmetric shedding of the forebody vortices. An added complication to this phenomenon is that the traditional control surfaces operating under this condition are ineffective in overcoming the yawing moment created by the side force because they are likely to be immersed in the wakes of the wings and the forebody. These combined effects are highly detrimental to the performance of the flight vehicle. Currently, numerous control devices have been proposed to overcome this problem, including 1) symmetric strakes[3,4] or active devices to create either blowing or suction[4–6] to induce symmetric separation at the two sides of the forebody; 2) helical[7] or boundary-layer trip[8,9] to prevent the formation of strong coherent leeward vortices, so as to reduce the side force; 3) small single strake at the leeward position of the nose[10,11] or just at the tip[12] to prevent vortex crowding, a situation that is thought to be responsible for hydrodynamic instability and, hence, flow asymmetry.

These devices have achieved some degree of success. For example, Bernhardt and Williams[13] found that it is possible to control both the magnitude and the direction of the side force using the suction method at $Re = 3 \times 10^4$. However, the range of applicability of these devices is usually limited, in many cases restricted by practical constraints such as space availability near the nose of the flight vehicle. Moreover, improperly installed strakes may lead to a worsening of the flow conditions. The single strake or symmetric strakes and trips must be installed symmetrically or they will have the opposite effect of generating a larger side force instead of reducing it. Similarly, pneumatic blowing or suction is found to be effective only when it is applied at certain optimal positions to influence the separation of the boundary layers.

The desire for a more effective control device has motivated us to carry out the present investigation. Our attention is focused primarily on two control devices that we have designed, based on the previous studies.

1) Helical or spiral grooves on the forebody are intended to force the boundary layer to separate at different angular positions along the axial direction. It is hoped that the nonuniformity of free shear layers in the axial direction will disrupt the formation of a discrete vortex core. However, it should be pointed that this is not a new idea. Rao[7] installed a pair of symmetric helical trips on two sides of a slender pointed forebody to suppress three-dimensional asymmetric vortices. However, for his device to work effectively, the trips must be installed symmetrically on the sides of the body. With our design, the helical grooves spiral around the nose tip and, therefore, are less sensitive to the roll angle.

2) Circular trips on the nose are used to trip the boundary layer into a transitional state. The idea is based on an earlier study by Lamont,[14] which shows that the side force can be reduced to a very small value in the transitional Reynolds number region (see also Keener and Chapman[1]). However, just like other protruding type of side force alleviation devices, the circular trips are expected to suffer from a larger drag penalty.

Received 26 April 1999; revision received 6 December 1999; accepted for publication 8 November 1999. Copyright © 2000 by the authors. Published by the American Institute of Aeronautics and Astronautics, Inc., with permission.

*Ph.D. Student, Department of Mechanical and Production Engineering, 10 Kent Ridge Crescent.

[†] Associate Professor, Department of Mechanical and Production Engineering, 10 Kent Ridge Crescent.

[‡] Associate Professor, Department of Mechanical and Production Engineering, 10 Kent Ridge Crescent.

[§] Senior Engineer, Aeronautics System Program, 20 Science Park Drive.

II. Experimental Apparatus and Techniques

Figure 1 shows a schematic of the experimental setup. The wind tunnel has a test section of 0.6 (height) $\times$ 1.0 m (width) and is operating at a freestream velocity U of 15 m/s, with a turbulence intensity of about 0.23%. The Reynolds number ($Re = UD/\nu$) based on the model base diameter D of 35 mm, is about 3.5×10^4, where ν is the kinematic viscosity of air. At this operating condition, the boundary layer involved was laminar because Lamont[14] has shown that boundary layer remains laminar below $Re = 2 \times 10^5$ for all angles of attack.

Figure 2 shows the dimensions of the clean, that is, without any control devices, tangent ogive nose cylindrical model used in the present investigation. The nose is $3.5D$ long and has a half-apex-angle δ_N of 16.25 deg. During fabrication, great care was taken to ensure the smooth transition from the nose section to the main body, which is $12.5D$ long. The model has an array of 72 pressure tapings, located at $2D$, $3D$, $4D$, $5D$, and $6D$ from the tip of the model. The first station, due to the space constraint, has only eight equally spaced pressure tapings (at 45 deg apart), whereas the other four stations have 16 tapings (at 22.5 deg apart) each. The locations of the pressure stations were arranged to cover at least the first peak of the local side force along the axial direction.[15] All surface pressure measurements were carried out using two sets of 48-channel scanivalves equipped with ± 0.3 psi pressure transducers. The accuracy of the transducer is about 0.2% of the full scale. This translates into a maximum error of ± 0.037 in the pressure coefficient at the operating wind speed. The surface pressures allowed the local side force distribution to be determined accurately. However, to determine the overall side force, a Nitta six-degree-of-freedom force balance was used. The balance is accurate up to ± 1.16 g, which corresponds to a maximum error of ± 0.0891 in the side force coefficient.

In the case of the helical grooves, a total of three geometries was tested (see Fig. 3a). Detail specifications of each model are shown in Table 1. In all cases, the grooves spiral in the axial direction for a distance of 60 mm (about $1.71D$) from the tip, and their depths are 5% of the local diameter.

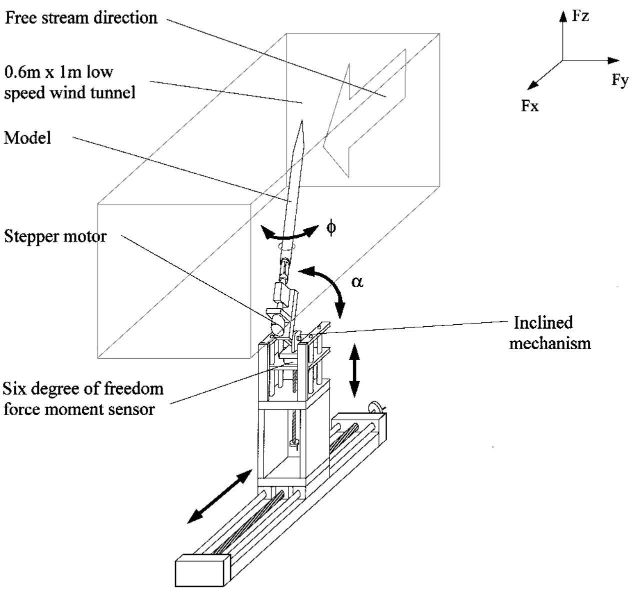

Fig. 1 Schematic diagram of the experimental setup.

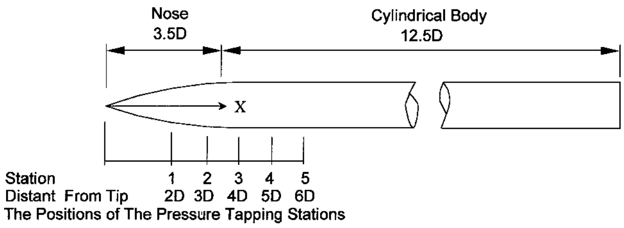

Fig. 2 Position of pressure taping stations on the model.

Table 1 Specifications of helical grooves

Designation	Specifications	Figure
Helical-1/1	One turn of helical groove of 1 mm wide	Fig. 3a(ii)
Helical-1.5/1	One turn of helical groove of 1.5 mm wide	Fig. 3a(iii)
Helical-1/3	Three turns of helical groove of 1 mm wide	Fig. 3a(iv)

Table 2 Specifications of the trips

Designation	Specifications	Figure
Trip-2.5D	Circular trip at $2.5D$ from the tip	Fig. 3b(i)
Trip-3.5D	Circular trip at $3.5D$ from the tip	Fig. 3b(ii)

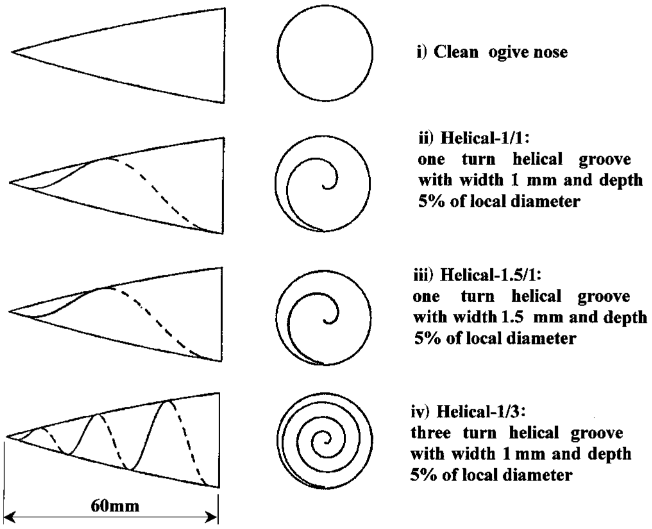

Fig. 3a Nose shapes.

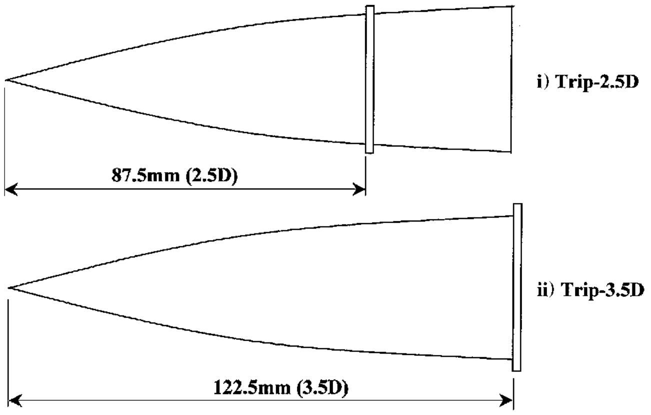

Fig. 3b Positions of circular trips on the ogive nose.

In addition, we also examine the effect of boundary-layer trips on the side force. The trips are actually circular brass rings that are 2 mm in width, and their heights are equivalent to 5% of the nose diameter at the locations where the rings attached (see Fig. 3b). Detail specifications of the trips are shown in Table 2.

Figure 4 defines the sign convention for the side force Fy, the roll angle ϕ, and azimuth angle θ. The positive side force is directed toward the starboard side of the body and normal to an incidence plane, that is, the plane defined by the body axis and the free-stream velocity vector. The azimuthal angle is designated zero at the most leeward position and increases in a counterclockwise direction (when viewed from the top, see Fig. 4). Note that the side force direction and the azimuth angle are fixed relative to the incidence plane of the body and do not change with the roll angle.

During the test, the model was rotated in a counterclockwise direction by a software-controlled stepper motor that was mounted behind the model. The motor was situated outside the test section (Fig. 1). The whole assembly was then mounted on an inclined mechanism that sat on the force balance. The inclined mechanism allowed the model to be pitched at different angle of attack α ranging from 20 to 80 deg.

Fig. 4 Definitions of side force *Fy*, roll angle ϕ, and azimuth angle θ.

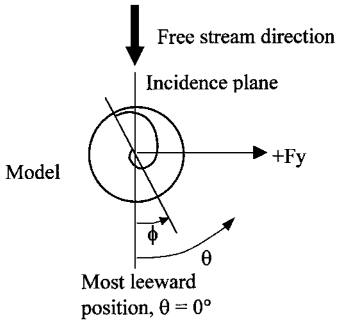

A computer equipped with a Pentium microprocessor was used to acquire the data as well as to control the stepper motor. A typical data acquisition routine first rotates the model to a new roll angle and, after allowing a 2-s delay for the flow to stabilize, acquires force data at a sampling frequency of 1 kHz over a 10-s period. This was followed immediately by the measurement of surface pressure at all of the 76 pressure tapings. Because of the limitation of the data acquisition card, pressure measurements had to be carried out consecutively using two sets of scanivalves. When all of the pressure readings were taken, the described procedure was repeated until all of the desired data were captured. For each angle of attack, measurements were carried out over the entire 360 deg roll-angle range, at a constant increment of 7.2 deg.

III. Results and Discussions

Figures 5–9 show the results for the three helical groove cylinders, and Figs. 10–14 show the corresponding results for the two tripped ogive cylinders. In all of the cases studied, the results are compared with the clean ogive nose results obtained under identical conditions and reported by Luo et al.[16]

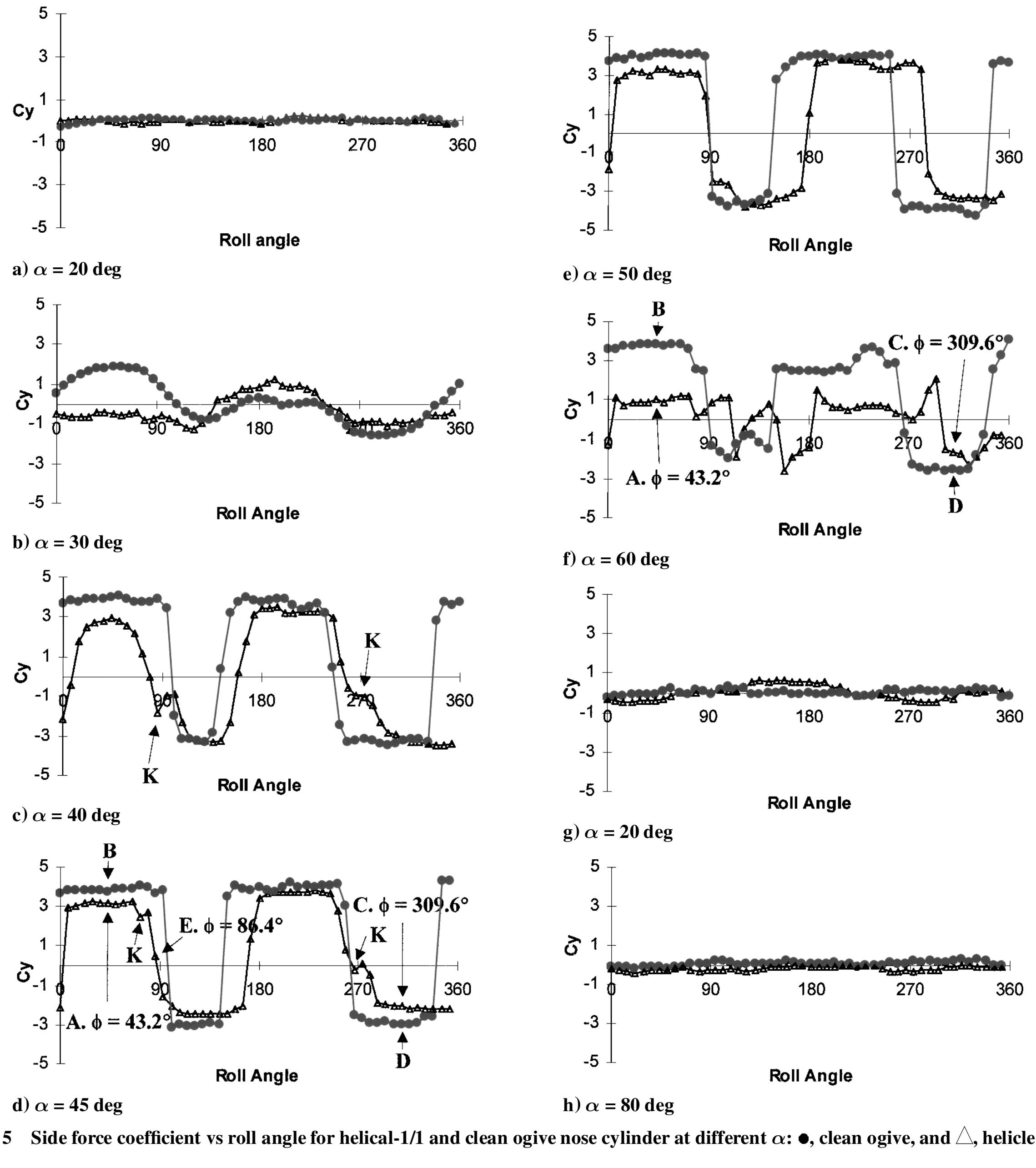

a) α = 20 deg

b) α = 30 deg

c) α = 40 deg

d) α = 45 deg

e) α = 50 deg

f) α = 60 deg

g) α = 20 deg

h) α = 80 deg

Fig. 5 Side force coefficient vs roll angle for helical-1/1 and clean ogive nose cylinder at different α: ●, clean ogive, and △, helicle-1/1.

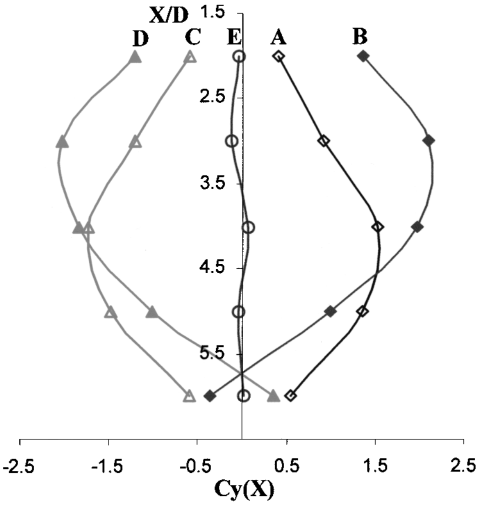

Fig. 6 Local side force distributions for helical-1/1 and the clean ogive nose at $\phi = 43.2$ and 309.6 deg and $\alpha = 45$ deg: ◇ A, helical-1/1 at 43.2 deg; ◆ B, clean ogive nose at 43.2 deg; △ C, helical-1/1 at 309.6 deg; and ▲ D, clean ogive nose at 309.6 deg; ○ E, helical-1/1 at 86.4 deg.

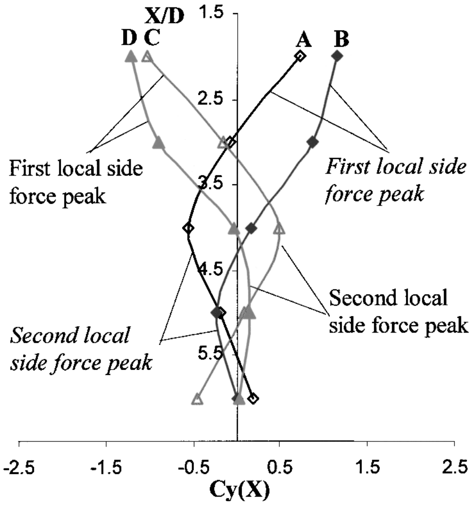

Fig. 7 Local side force distributions for helical-1/1 and the clean ogive nose at $\phi = 43.2$ and 309.6 deg and $\alpha = 60$ deg: ◇ A, helical-1/1 at 43.2 deg; ◆ B, clean ogive nose at 43.2 deg; △ C, helical-1/1 at 309.6 deg; and ▲ D, clean ogive nose at 309.6 deg.

Helical Grooves

Helical-1/1

Figure 5 shows the side force coefficient Cy distributions for helical-1/1 pitched at angles of attack ranging from 20 to 80 deg. Also shown is the corresponding distribution for the clean ogive nose. It is clear from Fig. 5 that the side force distributions are affected by the presence of the helical grooves, especially at angles of attack that are within the range of 30–70 deg. Outside this range, the influence of the grooves is rather small. On the whole, the helical-1/1 cylinder has a slightly lower maximum side force than the clean ogive nose at the same angle of attack. The most significant reduction occurs at $\alpha = 60$ deg. Detailed findings are discussed next.

When $40 < \alpha < 50$ deg, helical-1/1 appears to have delayed the formation of square-wave-like side force distribution to a higher angle of attack. This is clearly demonstrated in Figs. 5c and 5d. To obtain a clearer idea of the flow behavior when the body is subjected to the side forces, as indicated by points A–D in Fig. 5d, their respective local side force distributions are plotted in Fig. 6. Points A and B correspond to $\phi = 43.2$ deg whereas points C and D correspond to $\phi = 309.6$ deg. These local side forces are computed by integrating the surface pressure distributions at various measuring stations along the axial direction. From Fig. 6 it is obvious that the peaks of the local side force distributions on helical-1/1 is smaller than that on the clean ogive nose. This implies that the flow past helical-1/1 is relatively less asymmetric than the flow past the clean ogive nose at the aforementioned roll angles. In addition, the local side force distribution at $\phi = 86.4$ deg, where the overall side force is near zero, that is, point E in Fig. 5d, is plotted in Fig. 6. From Fig. 6, it is clear that the local side force at $\phi = 86.4$ deg is quite negligible, therefore, implying that the associated vortices are symmetrical. Thus, the near zero overall side force is not due to the cancellation of the local side forces of the opposite sign, as one may argue, but to the symmetry of the flow.

The side force of helical-1/1 has a more regular two-cycle variation with roll angle than that of the clean ogive nose, and the side force changes sign at an approximate roll angle interval of 90 deg. This suggests that helical-1/1 acts like a large imperfection on the nose; it reduces the side force acting on the cylinder by inducing disturbance to the flow and not by destroying the coherence of the vortices as it was intended to. The effects of perturbation on the nose have been studied thoroughly by Moskovitz et al.[17] and Degani and Tobak.[18] In the experiments of Moskovitz et al.,[17] cylindrical beads of varying height and diameter were attached to a cone/cylinder model and a 3.0 caliber tangent ogive model separately to represent a discrete surface perturbation. They found that the beads were able to influence the flow and vary the magnitude and the direction of side force, irrespective of the symmetry of the original flow. However, there is a reduction in the effectiveness of the bead with decreasing bead size and increasing distance from the tip. They suggested that the beads cause a discrete perturbation that influences the flowfield through three different mechanisms: 1) to bias the direction of the net circulation at the bead's axial location, 2) to trigger the boundary-layer transition, and 3) to disturb the flow at separation. Similarly, Degani and Tobak[18] examined the effects of disturbance on the flow past pointed bodies of revolution at incidence, by changing the size and location of the disturbance. They found that minute changes in the size or location of the controlled disturbance can result in finite changes in the asymmetric flowfield, even to the extent of reversing the sign of the side force or making its magnitude nearly zero. Although the effects of the helical groove on the flowfield in our experiment is more complicated than the discrete perturbations just discussed, it appears that the helical grooves also acts as a perturbation that overwhelms the effects of a more randomly distributed microimperfections on the model. The helical groove has the effect of biasing the orientation of the flow (depending on the orientation of the groove), as well as triggering its asymmetry. Furthermore, it is likely that the kinks (identified as K in Figs. 5c and 5d) that appear in the side force distribution when the roll angles are near 90 and 270 deg are caused by the groove's disturbance on the separation position(s) of the boundary layer(s).

As already mentioned, the effect of the helical groove on the side force is greatest when $\alpha = 60$ deg. For example, the maximum side force of helical-1/1 is nearly 50% lower than that on the clean ogive nose. Furthermore, the regular two-cycle side force distribution, which can be seen so clearly in Figs. 5d and 5e, is now replaced by a more random distribution in Fig. 5f. To get a better idea of the flow characteristics when $\alpha = 60$ deg, Fig. 7 shows the local side force distributions of helical-1/1 at $\phi = 43.2$ and 309.6 deg. For comparison, the corresponding results for the clean ogive nose are also shown. It can be seen that for the clean ogive nose model (curves B and D), the local side force varies in a damped sinusoidallike manner along the axial direction. This behavior has been attributed to the orientation and breakaway position of the shed vortices (see Lamont and Hunt[15] and Luo et al.[16]). For helical-1/1 (curves A and C), the same phenomenon occurs except that the vortex breakaway position appears to take place much closer to the tip, as can be inferred from the local side force distribution curves. Based on the areas under the curves it is evident that the relatively large second local side force peak has reduced the side force caused by the first peak, thus resulting in the smaller overall side force for the helical grooves.

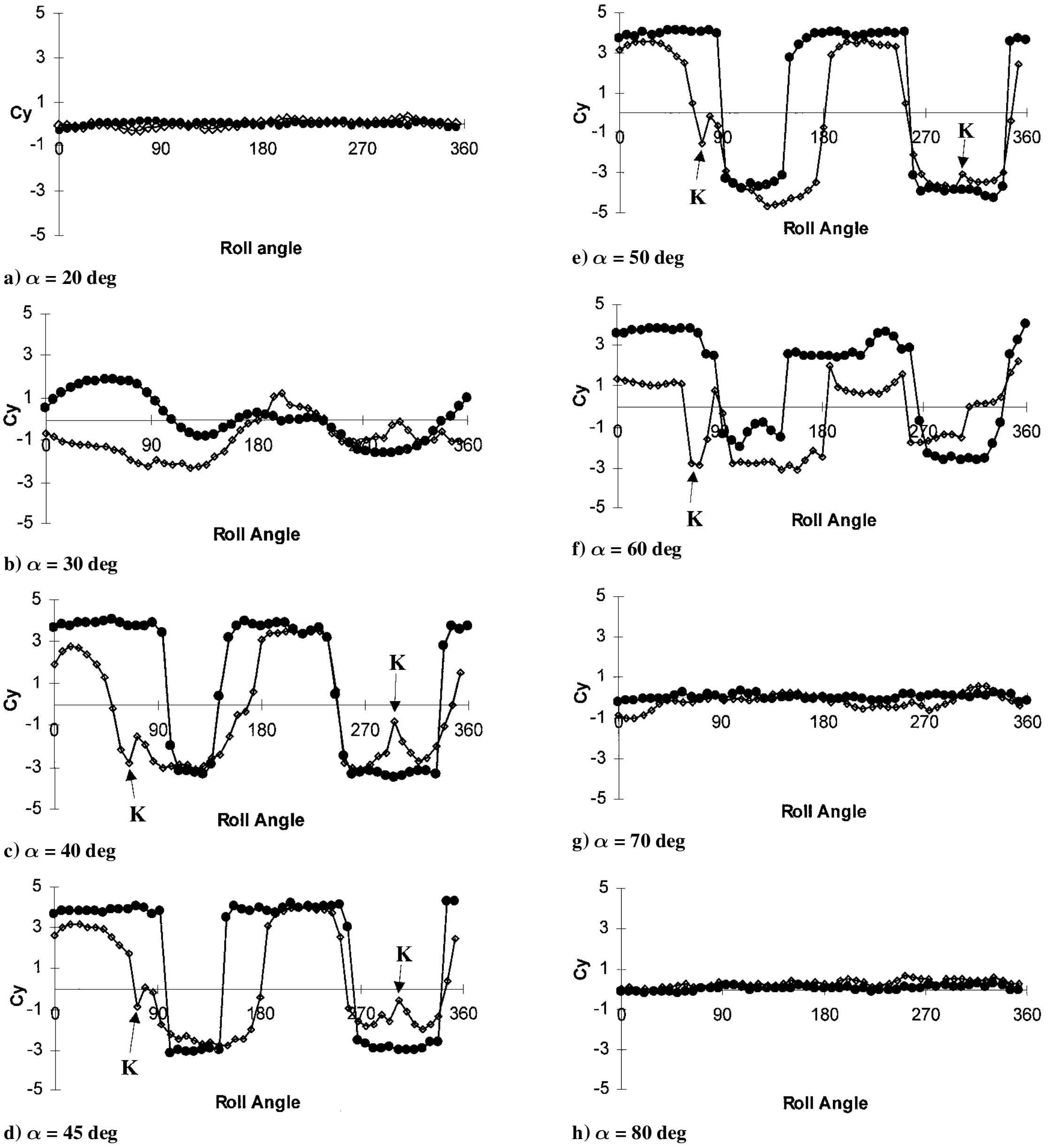

a) α = 20 deg

b) α = 30 deg

c) α = 40 deg

d) α = 45 deg

e) α = 50 deg

f) α = 60 deg

g) α = 70 deg

h) α = 80 deg

Fig. 8 Side force coefficient vs roll angle for helical-1.5/1 and clean ogive nose cylinders at different α: ●, clean ogive, and ◇, helical-1.5/1.

For angle of attack above 60 deg, the flow is dominated by periodic vortex shedding, and, therefore, the average side force tends to zero.

Helical-1.5/1

The effect of enlarging the width of the groove on the side force coefficient distributions is shown in Fig. 8. An obvious difference between this model and helical-1/1 is the delay of the square-wave-like side force distribution to a much larger angle of attack for this model. In fact, even when α is as high as 50 deg, there are still traces of sinusoidal-like variation in the side force distribution. What is interesting about this model is the presence of large kinks in the side force distribution at around $\phi = 72$ and 300 deg and $40 \leq \alpha \leq 60$ deg (K in Figs. 8c–8f). They are probably caused by the groove's disturbance on the separation point(s).

Helical-1/3

With the number of helical turns increased to three, the side force distribution is shown in Fig. 9. Surprisingly, having more turns does not appear to affect the force distribution as much as helical-1/1. In fact, the distribution is not significantly different from that of the clean ogive nose in the range $30 < \alpha < 60$ deg (Figs. 9c–9e). Interestingly, when at $\alpha \approx 60$ deg (Fig. 9f), there is a large reduction in the overall side force, similar to the two earlier models. In fact, the magnitude of the reduction of the present case is the largest among the three models. At this stage, no evident explanation is available for these contrary effects of helical-1/3.

Circular Trips

Trip-2.5D

Figure 10 shows the side force distribution of the trip-2.5D model, that is, circular trip at $X = 2.5D$, together with that of the clean ogive nose. From Fig. 10, it is quite obvious that the trip is more effective in alleviating the side force than the helical grooves discussed earlier. In fact, when $\alpha = 30$ deg (Fig. 10a), the maximum side force is reduced by more than 75% of the clean ogive nose. A detail picture of the effect of the trip on the flow behavior can be obtained from the surface pressure distribution. For example, when $\phi = 43.2$ deg (Fig. 10a), the pressure distributions at the five measuring stations are shown in Fig. 11a. For the purpose of comparison, the corresponding results for the clean ogive nose are shown in Fig. 11b. Here, it is clear that the two sets of results are quite similar except for stations 2 and 3, which are the stations located immediately

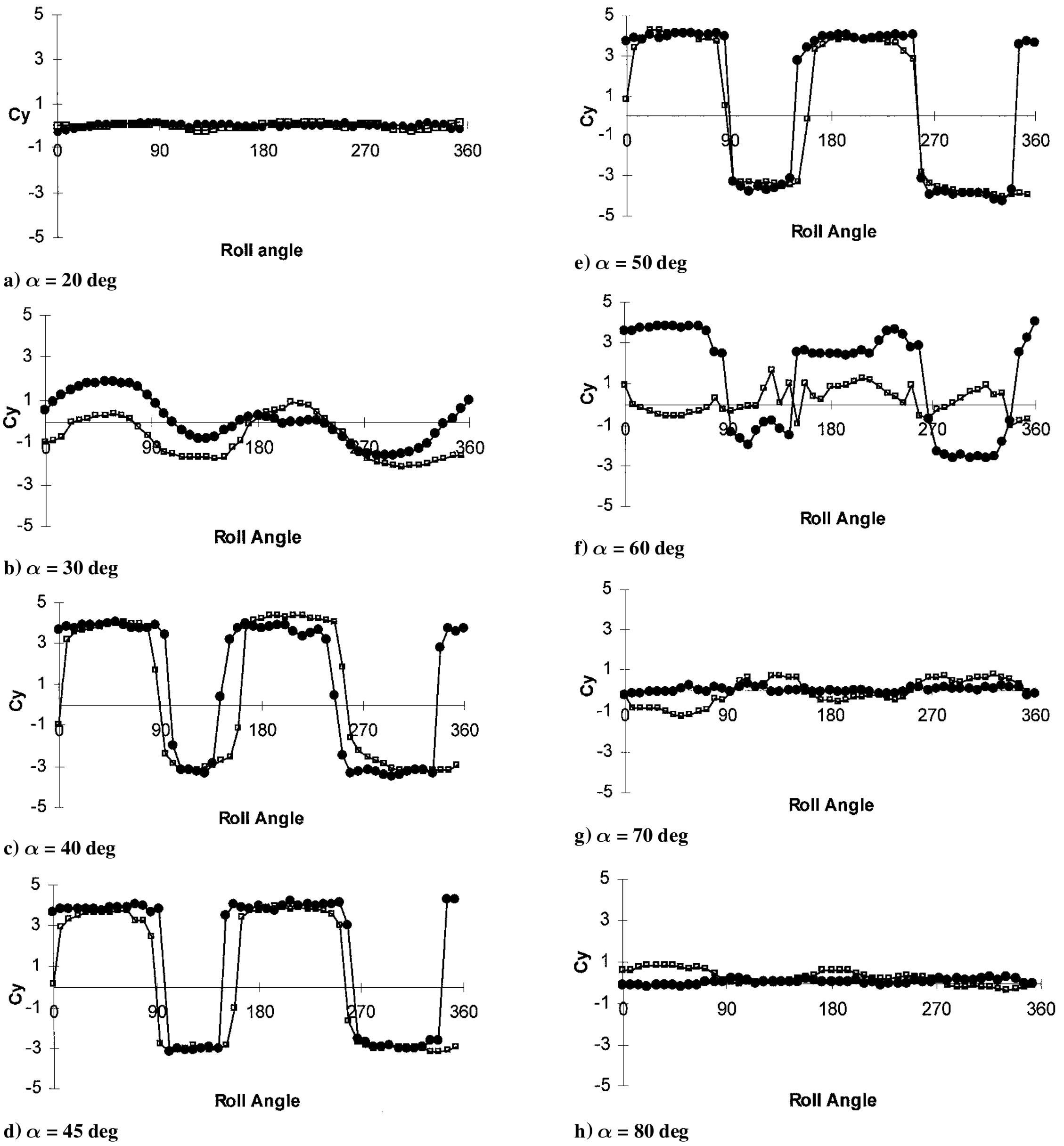

a) α = 20 deg

b) α = 30 deg

c) α = 40 deg

d) α = 45 deg

e) α = 50 deg

f) α = 60 deg

g) α = 70 deg

h) α = 80 deg

Fig. 9 Side force coefficient vs roll angle for helical-1/3 and clean ogive nose cylinders at different α: ●, clean ogive, and □, helical-1/3.

downstream of the trip. At these stations, the results show that the state of the boundary layer has been significantly altered by the trip, which causes a large change in the surface pressure, especially near the leeward part of the model. The trip also appears to have caused a considerable shift in the separation positions from $\theta = 90$ and 270 deg (also see Ref. 14) to $\theta = 45$ and 315 deg.

At angle of attack between 40 and 60 deg (Figs. 10b–10e), the side force on trip-2.5D is generally smaller than that of the clean ogive nose, and its distribution is also more random. The additional fluctuation in the side force on trip-2.5D could be caused by the near-transitional state of the boundary layer.

Another interesting feature shown in Fig. 10 is the phase relation between the two models. For example, when $\alpha = 40$ deg (Fig. 10b), the side force distributions of trip-2.5D are, with the exception of the first and the last half-cycle of the side force distribution, most of the time in-phase with that of the clean ogive nose. However, when α is increased to 45 deg (Fig. 10c), the side force distributions of the two models are out-of-phase, thus indicating that the side forces are in opposite directions. Interestingly, the side force distributions are in-phase again when the angle of attack is increased to 50 deg (Fig. 10d), but again become out-of-phase at $\alpha = 60$ deg (Fig. 10e). This phenomenon can be explained as follows: As the angle of attack is increased, it is well known that both the flow asymmetry and vortex breakaway propagate upstream. However, the position of the trip remains fixed. In other words, the position of the trip relative to the steady vortices changes with the angle of attack. This behavior can be clearly seen in the local side force distribution of both the tripped and the clean ogive nose models that are shown in Fig. 12 for the case of $\phi = 43.2$ deg and $\alpha = 40$–60 deg. It can be seen in Fig. 12a that at $\alpha = 40$ deg the local side force for the both cases are similar up to a distance of $X/D = 3$. Beyond this point, the distribution for trip-2.5D starts to deviate appreciably from that on the smooth nose cylinder and changes sign at a much shorter axial distance from the tip. It is likely that the trip at $X/D = 2.5$ plays a significant role here. Also, the magnitude of the first local side force peak for the trip-2.5D model is smaller than that of the clean ogive nose. This, coupled with the smaller axial extent of the first peak of the local side force distribution, leads to an overall side force that points in the direction opposite to that of the clean ogive nose (see arrow in Fig. 10b). At $\alpha = 45$ deg (Fig. 12b), the axial extent of the first local side force peak has decreased only slightly, but the second peak has propagated upstream considerably and is now smaller. Consequently, the side force acting on the model at 45 deg is slightly less than that at $\alpha = 40$ deg. At $\alpha = 50$ deg (Fig. 12c),

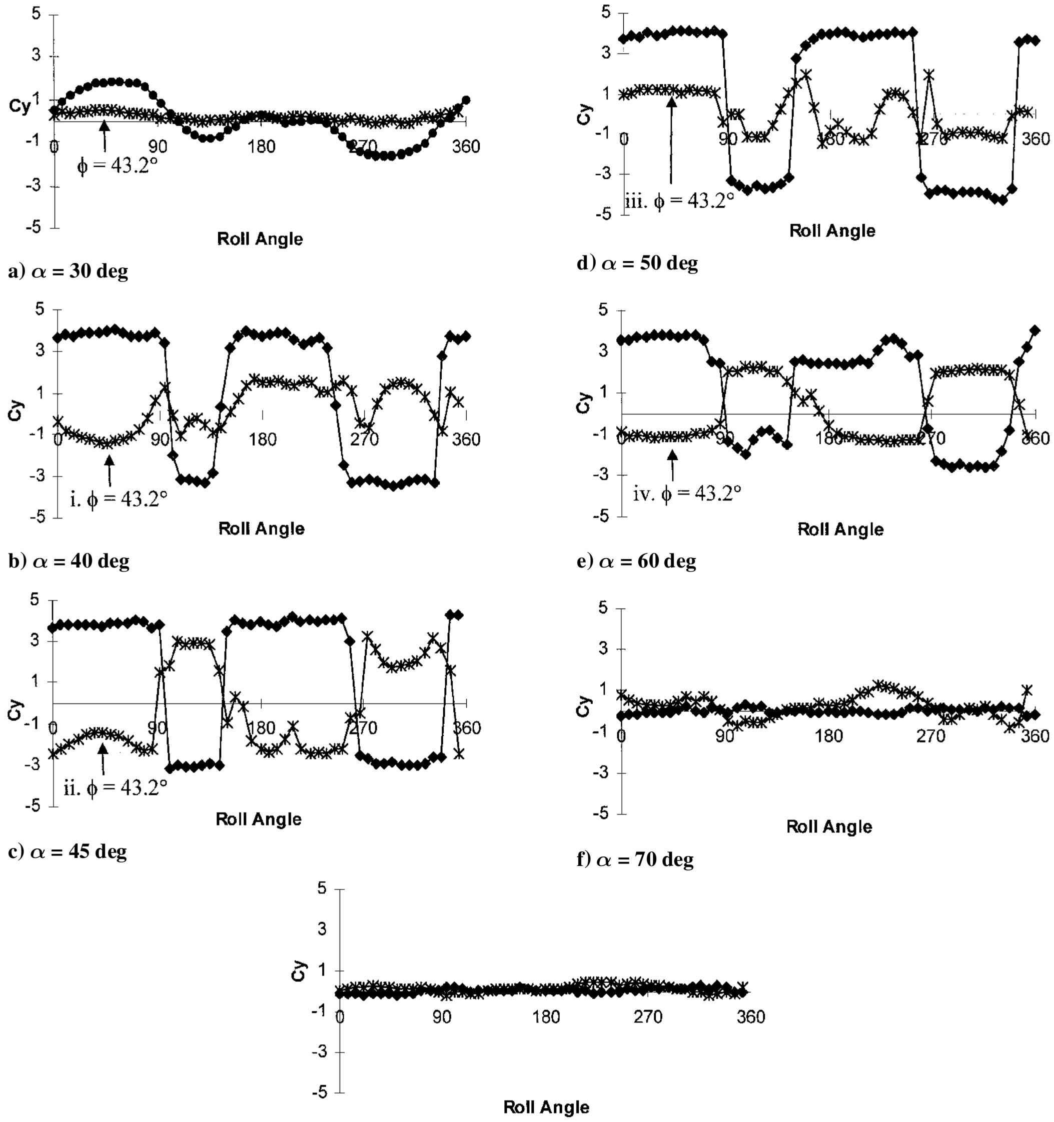

a) $\alpha = 30$ deg

b) $\alpha = 40$ deg

c) $\alpha = 45$ deg

d) $\alpha = 50$ deg

e) $\alpha = 60$ deg

f) $\alpha = 70$ deg

g) $\alpha = 80$ deg

Fig. 10 Side force coefficient vs roll angle for trip-2.5D and clean ogive nose at different α: ●, clean ogive nose, and $*$, trip-2.5D.

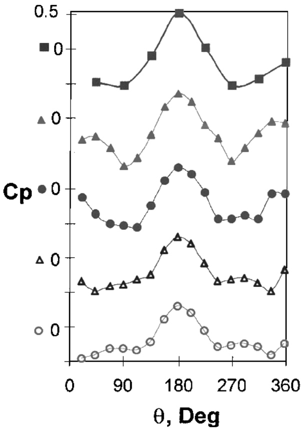

Fig. 11a Pressure coefficient vs θ for clean ogive nose at $\phi = 43.2$ deg and $\alpha = 30$ deg: ■, station 1; ▲, station 2; ●, station 3; △, station 4; and ○, station 5.

Fig. 11b Pressure coefficient vs θ for trip-2.5D at $\phi = 43.2$ deg and $\alpha = 30$ deg: ■, station 1; ▲, station 2; ●, station 3; △, station 4; and ○, station 5.

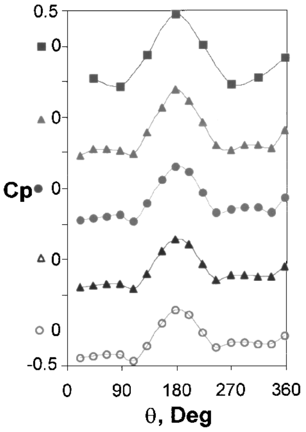

although the axial extent of the first local side force peak continues to decrease, the rate of decrease of the second local side force peak is much faster, and hence, the first local side force peak plays a more dominant role in the overall side force distribution. This explains why at $\alpha = 50$ deg the total side force still points in the same direction as that of the clean ogive nose, whereas at $\alpha = 40$ and 45 deg the direction is opposite. At $\alpha = 60$ deg (Fig. 12d), the effects of the trip on the vortices become more global in nature because it also affects the region upstream of it (the trip) as well. Here, the local side force up to $X/D = 3$ is almost zero, and therefore, the first peak effectively does not exist. It is, thus, obvious that the second peak is the dominating one here at $\alpha = 60$ deg. This explains why at $\alpha = 60$ deg the overall side force is pointing in the same direction as $\alpha = 40$ and 45 deg.

Trip-3.5D

When the circular trip was shifted farther away from the tip, it was found that the side force at all angles of attack was reduced. The

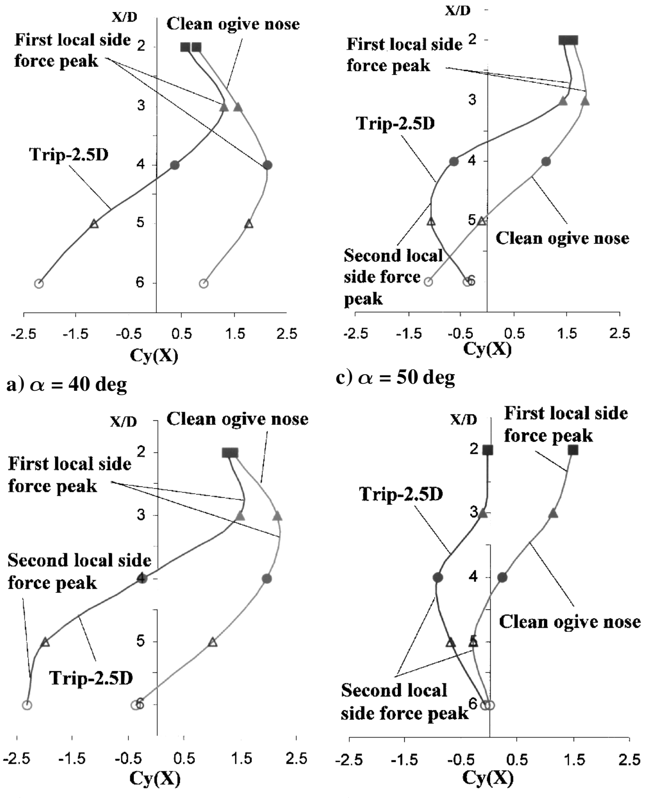

a) α = 40 deg

b) α = 45 deg

c) α = 50 deg

d) α = 60 deg

Fig. 12 Local side force distributions for trip-2.5D and the clean ogive nose at $\phi = 43.2$ deg and α from 40 to 60 deg.

only exception was at $\alpha = 70$ deg, where the side force was larger than that on the clean ogive nose (see Fig. 13). For this model, the maximum side force occurs at $\alpha \approx 50$ deg. The reduction in the side force is as much as 50% of that acting on the clean ogive nose. This suggests that it is more effective to locate the trip at $X = 3.5D$ than at $X = 2.5D$ because the latter only leads to a 25% reduction in the overall side force when compared to the clean ogive nose and the side force peaks at a slightly lower angle of $\alpha = 45$ deg. However, the negative effect of the trip-3.5D model is the presence of an appreciable side force (larger than that on trip-2.5D) at $\alpha = 70$ deg.

In Fig. 14, the local side force axial distributions at various angles of attack are presented. Here, it can be clearly seen that at $\alpha = 40$ and 45 deg (Figs. 14a and 14b), the local side force is only affected at $X/D = 5$ and 6, which are behind the trip. The first local side force peak is not significantly affected by the trip, and its magnitude is about the same as the second (opposite direction) local side force peak. Hence, the overall side force is smaller. At $\alpha = 50$ deg (Fig. 14c), the effects of the trip can be felt both upstream and downstream of the trip. This is different from the trip-2.5D model, where the upstream effect can be felt only when $\alpha = 60$ deg (Fig. 14d). This may be due to the greater height of trip-3.5D (5% of local diameter at $X/D = 3.5$) than trip-2.5D.

We now would like to compare the effectiveness of our helical groove and trip with devices used by others. This is shown in Fig. 15, where the side forces of helical-1/1, trip-3.5D, and the clean ogive nose at $\phi = 0$ deg are compared with the results of Rao[7] and Modi et al.[19] In Rao's experiment,[7] a pair of solder wires were deployed helically and symmetrically on the two sides of an ogive nose model. On the other hand, in the Modi et al.,[19] investigation, a helical trip with a pitch of 3 cm was installed on the nose of a cone nose cylinder to suppress the side force. It is obvious from Fig. 15 that the present helical groove is less effective in reducing the side force than the helical trips of Modi et al.[19] and Rao.[7] For example, the Modi et al.[19]

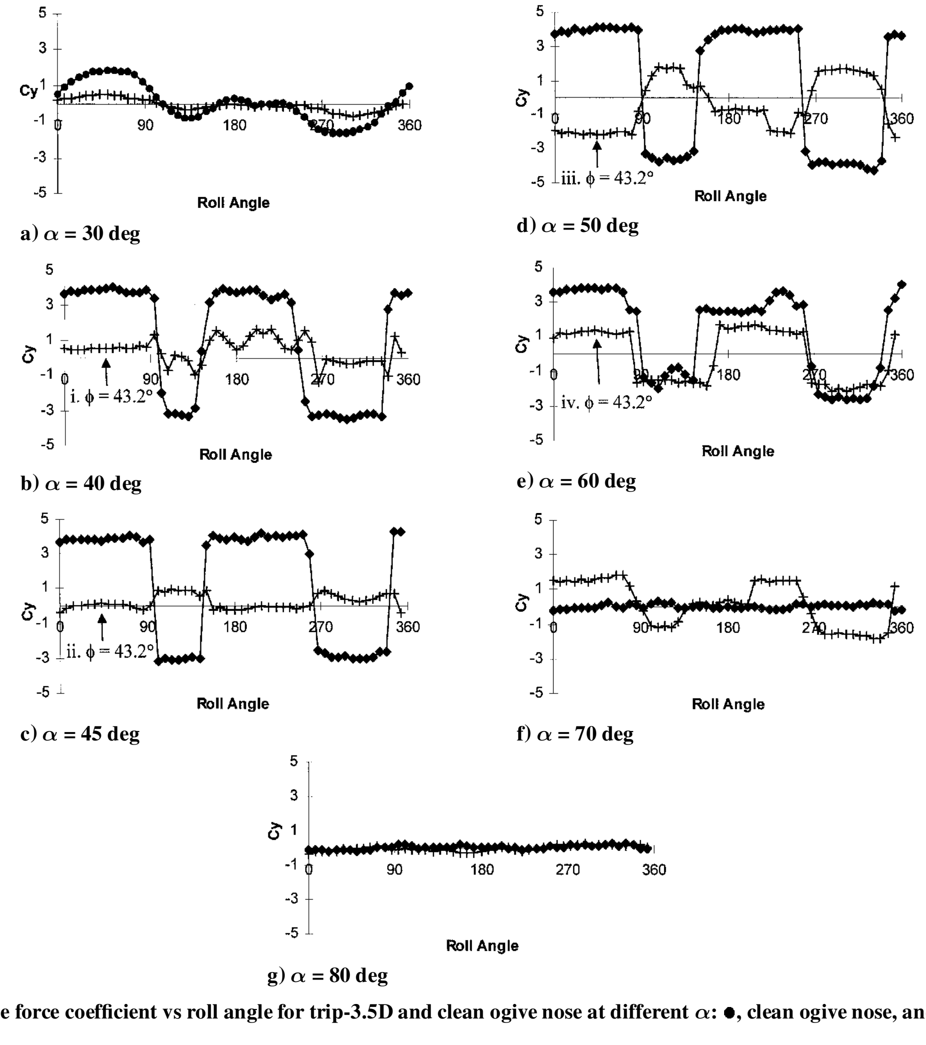

a) α = 30 deg

d) α = 50 deg

b) α = 40 deg

e) α = 60 deg

c) α = 45 deg

f) α = 70 deg

g) α = 80 deg

Fig. 13 Side force coefficient vs roll angle for trip-3.5D and clean ogive nose at different α: ●, clean ogive nose, and |, trip-3.5D.

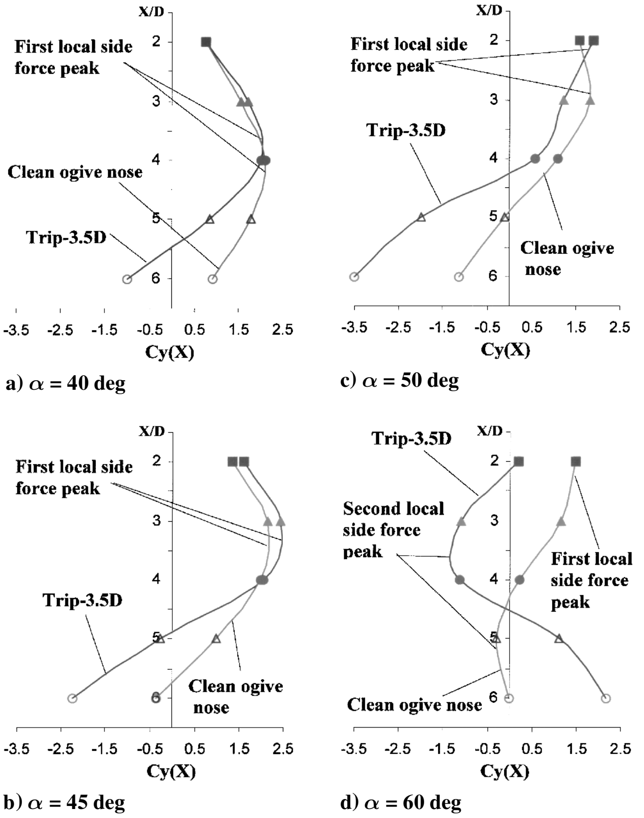

a) α = 40 deg

c) α = 50 deg

b) α = 45 deg

d) α = 60 deg

Fig. 14 Local side force distributions for trip-3.5D and the clean ogive nose at $\phi = 43.2$ deg and α from 40 to 60 deg.

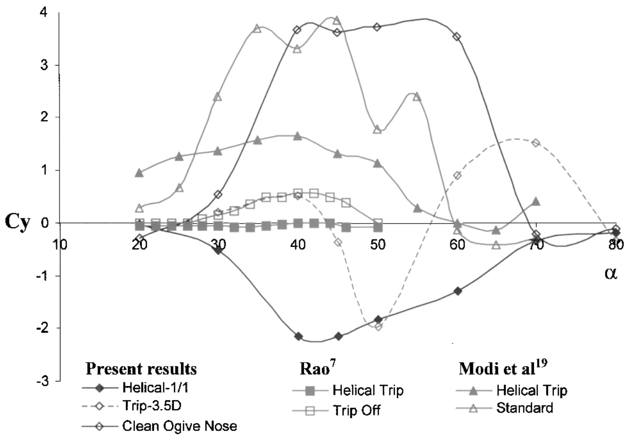

Fig. 15 Comparison of the present results with those of Rao[7] and Modi et al.[19]; note that roll angle $\phi = 0$ deg for the present results.

helical trip shows a reduction in the side force of as much as 60% of the clean ogive nose, whereas the symmetric helical trip of Rao[7] can reduce the side force to near zero. On the other hand, our helical-1/1 can only achieve at most a 51% side force reduction. Among the devices tested in the present study, trip-3.5D is found to be the most effective, except at $\alpha = 50$ and 70 deg. In hindsight, it is not surprising that the helical trip is more effective than the groove because the trips are extended into the flow, thus causing more perturbation than the grooves. On the other hand, protruded type of devices like trips are also almost certainly going to lead to drag penalty. With both side force reduction and minimum drag penalty simultaneously considered, devices like a helical groove may appear to some designers as the better overall compromise. However, the authors are not in the position to discuss this topic further because quantitative drag force data are not presently available.

IV. Conclusion

An experimental investigation to determine the effectiveness of the helical groove and circular trip on the side force characteristics of a tangent ogive cylinder has been carried out. The main findings are summarized as follows.

1) The present results suggest that the helical groove behaves more like a large perturbation on the nose by inducing disturbances into the flowfield, but the disturbance is not strong enough to completely destroy the vortex structures, as one may hope for.

2) With the helical-1/1 model, it is found that the groove does not have a significant influence on the onset of the side force. However, the groove appears to have delayed the appearance of the square-wave-like distribution of the side force to higher angle of attack. The greatest effect of the groove occurs when $\alpha = 60$ deg. At this incidence angle, a reduction of as much as 50% of the side force has been found.

3) With the helical-1.5/1 model, it is found that a 50% increase in the groove width has resulted in a further delay in the onset of the square-wave-like side force distribution to a much higher angle of attack of 50 deg.

4) Increasing the number helical turn to three (helical-1/3) diminishes the effectiveness of the groove in the range $30 \leq \alpha \leq 50$ deg. Interestingly, when $\alpha = 60$ deg, the groove causes more than 50% reduction in the side force when compared with the smooth model.

5) Of the two categories of control devices tested, that is, helical groove and circular trip, the circular trips are found to be more effective in triggering the transition of the separated shear layers, thus causing a larger reduction in the maximum side force.

6) At a given roll angle, the results show that the direction of the side force changes with the angle of attack. This is caused by changes in the relative magnitude of the first and the second local side force peak. Surprisingly, at α of about 70 deg, the side forces generated by both devices are larger than that of the clean ogive nose.

7) Although both the trips tested have significant effects on the destruction of the first vortex pair generated at the tip, their destruction is not sufficient to completely eliminate the side force because the existence of additional vortex pairs farther downstream may still create a significant side force.

8) On the whole, the helical and circular trips are found to be more effective in reducing the side force than the helical groove. However the trips are expected to suffer from a larger drag penalty.

References

[1] Keener, E. R., and Chapman, G. T., "Onset of Aerodynamic Side Force at Zero Sideslip on Symmetric Forebodies at High Angles of Attack," AIAA Paper 74-770, Aug. 1974.

[2] Keener, E. R., Chapman, G. T., and Kruse, R. L., "Effects of Mach Number and Afterbody Length on Onset of Asymmetric Forces on Bodies at Zero Sideslip and High Angle of Attack," AIAA Paper 76-66, Jan. 1976.

[3] Coe, P. L., Chambers, J. R., and Letko, W., "Asymmetric Lateral-Directional Characteristics of Pointed Bodies of Revolution at High Angles of Attack," NASA TN D-7095, 1972.

[4] Malcolm, G. N., and Ng, T. T., "Forebody Vortex Control as a Complement to Thrust Vectoring," Society of Automotive Engineers, Technical Paper Series 901851, 1990.

[5] Malcolm, G. N., "Forebody Vortex Control," AGARD R-776, 1991.

[6] Peake, D. J., and Owen, F. K., "Control of Forebody Three Dimensional Flow Separation," *Proceedings of the Aircraft Dynamics of High Angles of Attack: Experiments and Modelling*, CP-262-15, AGARD, March 1979, pp. 6-1–6-40.

[7] Rao, D. M., "Side-Force Alleviation on Slender, Pointed Forebodies at High Angles of Attack," *Journal of Aircraft*, Vol. 16, No. 11, 1979, pp. 763–768.

[8] Keener, E. R., Chapman, G. T., and Cohen, L., "Side Forces on a Tangent Ogive Forebody with a Fineness Ratio of 3.5 at High Angles of Attack and Mach Numbers from 0.1 to 0.7," NASA TM X-3437, Feb. 1976.

[9] Keener, E. R., Chapman, G. T., Cohen, L., and Taleghani, J., "Side Forces on Forebody at High Angles of Attack and Mach Numbers from 0.1 to 0.7: Two Tangent Ogives, Paraboloid and Cone," NASA TM X-3438, Feb. 1976.

[10] Stahl, W. H., "Suppression of Vortex Asymmetry Behind Circular Cones," *AIAA Journal*, Vol. 28, No. 6, 1990, pp. 1138–1140.

[11] Asghar, A., Stahl, W. H., and Mohmood, M., "Suppression of Vortex Asymmetry and Side Force on a Circular Cone," *AIAA Journal*, Vol. 32,

No. 10, 1994, pp. 2117–2120.

[12] Ng, T. T., "Effect of a Single Strake on the Forebody Vortex Asymmetry," *Journal of Aircraft*, Vol. 27, No. 9, 1990, pp. 844–846.

[13] Bernhardt, J. E., and Williams, D. R., "The Effect of Reynolds Number on Vortex Asymmetry About Slender Bodies," *Physics of Fluids A*, Vol. 5, No. 2, 1993, pp. 291–293.

[14] Lamont, P. J., "Pressure Around an Inclined Ogive Cylinder with Laminar, Transitional, or Turbulent Separation," *AIAA Journal*, Vol. 20, No. 11, 1982, pp. 1492–1499.

[15] Lamont, P. J., and Hunt, B. L., "Pressure and Force Distributions on an Sharp-Nosed Circular Cylinder at Large Angles of Inclination to a Uniform Subsonic Stream," *Journal of Fluid Mechanics*, Vol. 76, No. 3, 1976, pp. 519–559.

[16] Luo, S. C., Lim, T. T., Lua, K. B., Chia, H. T., Goh, E. K. R., and Ho, Q. W., "Flowfield Around Ogive/Elliptic-Tip Cylinder at High Angle of Attack," *AIAA Journal*, Vol. 36, No. 10, 1998, pp. 1778–1787.

[17] Moskovitz, C. A., Hall, R. M., and DeJarnette, F. R., "Effects of Nose Bluntness, Roughness and Surface Perturbations on the Asymmetric Flow Past Slender Bodies at Large Angles of Attack," AIAA Paper 89-2236, Aug. 1989.

[18] Degani, D., and Tobak, M., "Experimental Study of Controlled Tip Disturbance Effect on Flow Asymmetry," *Physics of Fluids A*, Vol. 4, No. 12, 1992, pp. 2825–2832.

[19] Modi, V. J., Ries, T., Kwan, A., and Leung, E., "Aerodynamics of Pointed Forebodies at High Angles of Attack," *Journal of Aircraft*, Vol. 21, No. 6, 1984, pp. 428–432.